Plasmon polaritons in nanoparticle supercrystals: Microscopic quantum theory beyond the dipole approximation

Eduardo B. Barros,[1] Bruno Gondim Vieira,[1] Niclas S. Mueller,[2] and Stephanie Reich[2]
[1]*Department of Physics, Federal University of Ceará, Fortaleza, Ceará, 60455-760, Brazil*
[2]*Department of Physics, Freie Universität Berlin, Arnimallee 14, D-14195 Berlin, Germany*

Crystals of plasmonic metal nanoparticles have intriguing optical properties. They reach the regimes of ultrastrong and deep strong light-matter coupling, where the photonic states need to be included in the simulation of material properties. We propose a quantum description of the plasmon polaritons in supercrystals that starts from the dipole and quadrupole excitations of the nanoparticle building blocks and their coupling to photons. Our model excellently reproduces the results of finite difference time domain simulations. It provides detailed insight into the emergence of the polariton states. Using the example of a face centered cubic crystal we show that the dipole and quadrupole states mix in many high-symmetry directions of the Brillouin zone. A proper description of the plasmon and plasmon-polariton band structure is only possible when including the quadrupole-derived states. Our model leads to an expression of the reduced coupling strength in nanoparticle supercrystals that we show to enter the deep strong-coupling regime if the metal nanoparticles take up >60% of the total volume. In addition to the plasmon-polariton energies, we analyze the relative contributions of the dipole, quadrupole, and photonic states to their eigenfunctions and are able to demonstrate the decoupling of light in the deep strong-coupling regime. Our results pave the way for a better understanding of the quantum properties of metallic nanoparticle supercrystals in the ultrastrong- and deep strong-coupling regime.

I. INTRODUCTION

Nanoparticle supercrystals are three-dimensional lattices of nanoparticles with long-range crystalline order [1–7]. They have long fascinated physicists, chemists, and material scientists, because they promise material properties that cannot be found in nature [2]. Supercrystals are tailored through a particle-particle interaction and the choice of their building blocks. Initially, the discussion focused on collective vibrational and electronic modes of supercrystals made from semiconducting nanoparticles [8], but interest recently turned to collective optical excitations [9], especially when using metallic nanoparticles as the supercrystal building blocks [6,7,10–12]. The optical properties of metallic nanoparticle supercrystals are dominated by the response of their free electrons. When light interacts with a metallic nanoparticle, it excites localized surface plasmons—the collective oscillation of the free electrons—that strongly absorb and scatter light [13–15]. Plasmons of different nanoparticles interact in supercrystals over various length scales creating coherent collective excitations that propagate through the lattice [6,16,17]. The collective plasmonic modes couple to photons forming hybrid quasiparticles called plasmon polaritons [18]. Supercrystal plasmon polaritons differ greatly in their properties from the excitations of the individual nanoparticles, as they determine the optical response of metallic supercrystals, and open new pathways for scientific discoveries and technological developments [6,8,19,20].

Recently, we showed that plasmonic supercrystals can be used to explore phenomena in the ultrastrong regime of light-matter coupling (USC) [6,10,21]. In this regime the coupling strength is a considerable fraction of the bare frequency of the system, which leads to peculiar properties of the polariton states [22,23]. For interparticle gaps much smaller than the nanoparticle size, light-matter coupling even enters the regime of deep strong coupling (DSC) [6], where the interaction between light and matter exceeds the energies of the bare excitation. This means that the properties of plasmonic nanoparticle supercrystals can only be modeled when considering the existence of photonic states [6]. This is in sharp contrast to the standard treatment of light as an external perturbation. The DSC regime, moreover, promotes a wide range of exquisite and interesting physical effects such as a decoupling of light and matter and the breakdown of the Purcell effect [6,24], the squeezing of the photonic components of the polaritons, super-Poissonian phonon and photon statistics [25], and ground state electroluminescence [22,23,26]. Although most of these properties can be understood in terms of the Hopfield model for light-matter interactions [27], a microscopic model that is capable of making predictions for a specific plasmonic supercrystal is highly desirable.

Weick *et al.* [28] and Lamowski *et al.* [17] developed a quantum-based formalism that describes the polaritons of plasmonic supercrystals. The microscopic structure of the supercrystal and the dipole-dipole interactions between the nanoparticles turned out to be key for modeling the collective plasmon modes [17]. The model uses two common approximations that appear very reasonable on first sight, but turn out to limit its applicability: It considers only the dipole excitation of plasmonic nanoparticles and neglects

Umklapp processes when crossing the boundary of the Brillouin zone. The restriction to the dipole excitation is motivated by the small size (<100 nm) of plasmonic nanoparticles that prohibits the excitation of higher-order electrical modes in individual particles [15,29]. This argument, while correct, misses that higher-order modes of individual nanoparticles combine into dipole-active eigenstates in plasmonic oligomers and supercrystals [30,31]. These states may couple to the dipole-induced collective plasmons and the electromagnetic states affecting the final polariton dispersion. Umklapp processes are usually negligible for optical excitations, because the wavelength of visible light (500 nm) is small compared to the translational periodicity in natural crystals (0.1 nm). The unit cell of supercrystals, however, becomes a sizable fraction of the light wavelength, since nanoparticle diameters are several 10–100 nm. The quasistatic approximation breaks down and Umklapp processes may turn out to be important.

In this paper we develop a microscopic quantum model for plasmon polaritons in metallic supercrystals that includes quadrupolar plasmonic excitations and Umklapp processes. We validate it by a comparison to finite difference time domain (FDTD) simulations. Our model very well describes plasmon polaritons for supercrystals with low and high packing densities. We calculate the plasmon band structure for face centered cubic (fcc) supercrystals as a function of packing density showing that the quadrupole-derived collective eigenmodes cross and mix with the dipole-induced states for high packing densities. Including the coupling to the electromagnetic states results in plasmon polaritons in the USC and DSC regimes. The strongest contribution to light-matter coupling arises from the dipole plasmons; the quadrupole-photon coupling is an order of magnitude weaker than the dipole-photon interaction. However, the quadrupole contribution is important for the polariton band structure, because the energies of the collective plasmons are overestimated by several 100 meV at the Brillouin zone boundary when neglecting the quadrupole modes. We derive a closed expression for the reduced coupling strength and show that it mainly depends on the metal fill fraction. We extract the dipole, quadrupole, and photon contribution to all polariton states. The decoupling of light and matter clearly manifests as the three quasiparticles dominate distinct polariton branches in the DSC regime.

This paper is organized as follows: In Sec. II, we describe the theoretical framework and apply it to a three-dimensional Bravais lattice of spherical metallic nanoparticles. The theory for arbitrary crystal structures is given in the Supplemental Material (SM) [32]. We compare the calculated polariton dispersion to FDTD simulations. In Sec. III we calculate the plasmon and plasmon-polariton band structure of fcc supercrystals. We demonstrate how quadrupole modes and light-matter coupling affect the polariton dispersion. We discuss the properties of polaritons, the reduced coupling strength, and demonstrate the decoupling of light and plasmons in the DSC regime. In Sec. IV we summarize the main findings of the paper.

II. QUANTUM MICROSCOPIC PLASMON-POLARITON MODEL

In this section we derive the microscopic model of plasmon polaritons in metallic supercrystals. We first present a

general theoretical framework that describes individual and interacting nanoparticles with dipole and quadrupole excitations and their coupling to an electromagnetic field. This description is then applied to a Bravais lattice; we verify its validity and limitations by comparing to FDTD simulations of fcc nanoparticle crystals. Our microscopic quantum plasmon-polariton model contains the nanoparticle quadrupole in addition to their dipole excitations. Adding the quadrupole terms was challenging, because the quantum description of the light-matter interaction is based on the dipole approximation. One difficulty we encountered was to find a proper description of the conjugate momenta for higher-order multipoles. This problem dates back to the description of nuclear excitations and was discussed first by Bohr and Mottelson [33]. In 1978 Gulshani finally provided a formal development of canonically conjugate momenta for quadrupolar excitations [34], but no solution has been found for higher-order multipoles.

We start from the most general Hamiltonian for a set of charges distributed in space interacting with the electromagnetic field,

$$\mathcal{H} = \sum_n \frac{1}{2m}[\vec{p}_n - q_n\vec{A}(\vec{r}_n, t)]^2 + V_{\text{Coul}} + \mathcal{H}_L, \quad (1)$$

where V_{Coul} is the Coulomb interaction between the different n charges q_n in the system, $\mathcal{H}_L$ is the quantized free-electromagnetic field Hamiltonian, and $\vec{p}_n$ is the conjugate momentum to $\vec{r}_n$. $\vec{A}$ is assumed to be in the Coulomb gauge. We consider an isolated spherical metallic nanoparticle at the origin. The charges are bound by the nanoparticle volume, such that the summation n in Eq. (1) is restricted to the free electrons in the particle. We define a set of variables

$$h_\sigma = \frac{1}{N}\sum_n r_{n,\sigma}, \quad H_\gamma = \frac{1}{N\bar{\rho}}\sum_{n,\alpha,\beta} r'_{n,\alpha} r'_{n,\beta} \chi^\gamma_{\alpha\beta}, \quad (2)$$

where h_σ represents the center of mass displacement along the σ direction and is associated with the dipole moment of the charge distribution. $n = 1, \ldots, N_j$ runs through all the charges in a given nanoparticle. The second term H_γ is associated to the quadrupole moment, with α and β being different Cartesian directions. γ specifies one of the five possible quadrupolar modes, and $r'_{n\alpha} = r_{n,\alpha} - h_\alpha$. $\bar{\rho} = \langle 1/N \sum_n r_n^2 \rangle \sim \sqrt{\frac{2}{5}}\rho$, with ρ the radius of the spherical particle, is the expectation value of the diagonal term of the quadrupole moment. The respective conjugate momenta are

$$\pi_\sigma = \sum_n p_{n,\sigma}, \quad \Pi_\gamma = \frac{1}{\bar{\rho}}\sum_{n,\alpha,\beta} p'_{n,\alpha} r'_{n,\beta} \chi^\gamma_{\alpha\beta}, \quad (3)$$

with $p'_{n,\alpha} = p_{n,\alpha} - \pi_\alpha$. It should be mentioned that only the dipole part of this transformation is formally canonical. As discussed in the SM, the quadrupole term can only be associated with a canonical transformation (and thus with the expected commutation relations) if the total angular momentum of the charge distribution is zero and if the charge displacements are small compared to the bulk charge [34]. With these two considerations, the dynamical variable $\sum_n r_{n,\alpha}^2$ can be substituted by its expectation value $\bar{\rho}$ and the quadrupolar moments can be described in terms of the traceless and symmetric 3×3 matrices χ_γ which act as unit

tensors within the dyadic double-dot product (see SM). With this approximation, we can write the following inverse transformation for the quadrupolar canonical variables,

$$\sum_{n,\alpha,\beta} r_{n,\alpha} r_{n,\beta} = N \bar{\rho}^2 \left(\mathbf{1} + \frac{1}{\bar{\rho}} \sum_{\gamma} H_{\gamma} \chi_{\gamma} \right),$$

$$\sum_{n,\alpha,\beta} p_{n,\alpha} r_{n,\beta} = \bar{\rho} \sum_{\gamma} \Pi_{\gamma} \chi_{\gamma}. \quad (4)$$

Here, $\mathbf{1}$ is the 3×3 unit matrix.

We now consider a system of many nanoparticles. If there is no charge exchange between different particles, the full Hamiltonian of the system will be given by Eq. (1) but with the summation in n being extended to a summation for each particle $n \in j$ and a summation of the different particles in the system. With this, the matter Hamiltonian ($\mathcal{H}_M = \sum_n \frac{p_n^2}{2m} + V_{\text{Coul}}$) can be written as

$$\mathcal{H}_M = \mathcal{H}_M^D + \mathcal{H}_M^Q + \mathcal{H}_{\text{plpl}} + \mathcal{H}_M^{\text{HO}}, \quad (5)$$

where $\mathcal{H}_M^D + \mathcal{H}_M^Q$ represents the Hamiltonians for each nanoparticle in the system, including the kinetic energy associated with each of the canonical coordinates (D for dipole and Q for quadrupole) and the intraparticle Coulomb interactions. Both are assumed to be described in terms of harmonic oscillations with characteristic frequencies $\omega_{j,D}$ and $\omega_{j,Q}$, which can have different values for each nanoparticle j in the system. The term $\mathcal{H}_M^{\text{HO}}$ represents the dynamics of the higher-order coordinates, which are disregarded in the present model.

The plasmon-plasmon interaction between the different particles in the system is

$$\mathcal{H}_{\text{plpl}} = \mathcal{H}_{DD} + \mathcal{H}_{DQ} + \mathcal{H}_{QQ}, \quad (6)$$

corresponding to the dipole-dipole $\mathcal{H}_{DD}$, dipole-quadrupole $\mathcal{H}_{DQ}$, and quadrupole-quadrupole interaction $\mathcal{H}_{QQ}$. Explicit expressions for these terms are given in the Supplemental Material [32].

The characteristic size of plasmonic nanoparticles is 10–100 nm. Compared to atoms and molecules, the particle diameters are a considerable fraction of the light wavelength. The common approach for the light-matter interaction of expanding the vector potential in a Taylor series in the vicinity of the charge distribution and disregarding higher-order terms in k will not be effective. We perform the expansion in a slightly different way; we start from the vector potential of a plane wave given by

$$A_\lambda(\vec{r}, t) = \sum_{\vec{q}} A_{\vec{q}, \lambda}(t) \exp(i\vec{q} \cdot \vec{r}), \quad (7)$$

where λ specifies the light polarization and $\vec{q}$ is a vector in reciprocal space—not to be confused with the charges q. With this, the general light-matter interaction for a particle j can be separated into two parts. The first-order part,

$$\mathcal{H}_{LM}^{(1)} = -\frac{q_e}{m_e} \sum_{j,(n \in j), \lambda, \vec{q}} p_{n\lambda} A_{\vec{q}\lambda} \exp(i\vec{q} \cdot \vec{r}_n), \quad (8)$$

corresponds to the interaction of light with excitations of the electric charge distribution. The time dependence of $\vec{A}$ is

implicit. The second-order part,

$$\mathcal{H}_{LM}^{(2)} = \frac{q_e^2}{2m_e} \sum_{j, n \in j, \lambda, \vec{q}, \vec{q}'} A_{\vec{q}'\lambda}^* A_{\vec{q}\lambda} \exp[i(\vec{q} - \vec{q}') \cdot \vec{r}_n], \quad (9)$$

describes the back reaction of the electric field as it accelerates the electric charges [35]. This term is known as the A^2 term in the light-matter Hamiltonian; it becomes extremely important in the USC and DSC coupling regime [6,22].

Let us now take the spherical harmonic expansion of the plane wave around the position $\vec{R}_j$ of each nanoparticle in the system,

$$\exp(i\vec{q} \cdot \vec{r}_j) \sim j_0(qr_j) + 3i \frac{j_1(qr_j)}{qr_j} \vec{q} \cdot \vec{r}_j, \quad (10)$$

where $\vec{r}_j = \vec{r} - \vec{R}_j$ and we have retained only the lower-order terms. We apply this expansion to the first-order part of the light-matter interaction for each nanoparticle j independently and sum to get the full Hamiltonian. It then has a dipolelike contribution,

$$\mathcal{H}_{LM}^{(D,1)} = -\frac{q_e}{m_e} \sum_{j, \lambda, \vec{q}} A_{\vec{q}\lambda} \exp(i\vec{q} \cdot \vec{R}_j) \sum_{n \in j} p_{n\lambda} j_0(qr_{n,j}), \quad (11)$$

and a quadrupolarlike term,

$$\mathcal{H}_{LM}^{(Q,1)} = -\frac{q_e}{m_e} \sum_{j, \lambda, \vec{q}, \alpha, \beta} iq A_{\vec{q}\lambda} \exp(i\vec{q} \cdot \vec{R}_j)$$
$$\times (\hat{e}_\lambda \hat{e}_q : \hat{e}_\alpha \hat{e}_\beta) \sum_{n \in j} \frac{3j_1(qr_n)}{qr_n} p_{n\alpha} r_{n\beta}, \quad (12)$$

where (:) stands for a double-dot dyadic product. We now substitute $j_0(qr_n)$ and $3j_1(qr_n)/qr_n$ by their mean values in each nanoparticle,

$$\mathrm{f}_D = \langle j_0(qr_j) \rangle = \frac{3}{(q\rho_j)^3} [\sin(q\rho_j) - q\rho_j \cos(q\rho_j)] \quad (13)$$

and

$$\mathrm{f}_Q = \left\langle \frac{3j_1(qr_n)}{qr_n} \right\rangle = \frac{9}{(q\rho_j)^3} [\mathrm{Si}(q\rho_j) - \sin(q\rho_j)], \quad (14)$$

where $\mathrm{Si}(x)$ is the sine integral function. f_D and f_Q are nanoparticle form factors somewhat similar to the atomic form factors in x-ray diffraction theory [36]. The magnitude of the form factors decreases with increasing $q\rho$, effectively cutting off the contribution of photons with wave vectors much larger than $1/\rho$ to the light-matter interaction. This effect stems from the field retardation within the nanoparticle.

With this definition the first-order term in the light-matter interaction Hamiltonian becomes

$$\mathcal{H}_{LM}^{(D,1)} = -\sum_{j, \vec{q}} \mathrm{f}_D(q) \frac{Q_D}{M} \vec{\pi}_j \cdot \vec{A}_{\vec{q}, \vec{R}_j} \quad (15)$$

and

$$\mathcal{H}_{LM}^{(Q,1)} = \sum_{j, \vec{q}} \mathrm{f}_Q(q) \frac{Q_Q \bar{\rho}_j}{M} \Pi_{j, \nu} [\chi_\nu : \vec{q} \vec{A}_{\vec{q}, \vec{R}_j}], \quad (16)$$

where M is the total mass of the charges ($M = Nm_e$), Q_D and Q_Q are the screened dipole and quadrupole effective charges,

which will depend on the relative permittivity of the surrounding medium, and $\vec{q}\vec{A}_{\vec{q},\vec{R}_j}$ is a dyadic, with $\vec{A}_{\vec{q},\vec{R}_j} = \vec{A}_{\vec{q}}\exp(i\vec{q}\cdot\vec{R}_j)$). Note that for small nanoparticle radii (ρ) the form factors approach unity and the plasmon-photon interaction obtained by applying Taylor's expansion is recovered. In that case, the first-order light-quadrupole interaction increases linearly with q. For the second-order term, associated to the A^2 light-matter interaction term, we have the two contributions

$$\mathcal{H}_{LM}^{(D,2)} = \sum_{j,\vec{q},\vec{q}'} \mathrm{f}_D(q)\mathrm{f}_D(q')\frac{\mathrm{Q}_D^2}{2M}\left[\vec{A}_{\vec{q}',\vec{R}_j}^* \cdot \vec{A}_{\vec{q},\vec{R}_j}\right], \quad (17)$$

$$\mathcal{H}_{LM}^{(Q,2)} = \sum_{j,\vec{q},\vec{q}'} \mathrm{f}_Q(q)\mathrm{f}_Q(q')\frac{\mathrm{Q}_Q^2\bar{\rho}_j^2}{2M}\left[\vec{A}_{\vec{q}',\vec{R}_j}^* \vec{q}' \cdot \vec{q}\vec{A}_{\vec{q},\vec{R}_j}\right]. \quad (18)$$

The terms involving products between $\vec{A}_{\vec{q}}$ and $\bar{\nabla}\vec{A}_{\vec{q}}$ are disregarded, as the expectation value $\langle\sum_n \vec{r}_n\rangle = 0$ vanishes. Also, all nonquadratic terms, involving more than two dynamical variables, are disregarded within this approximation.

A. Plasmonic nanoparticle crystals

We now apply the proposed quantum mechanical description of light-matter coupling with dipole and quadrupole modes to a crystal of identical spherical nanoparticles placed in a Bravais lattice. The position of a nanoparticle in the crystal is determined by a lattice vector $\vec{R}$, and the index j is dropped. The model can be trivially extended to crystals with an arbitrary basis—see Supplemental Material for the equations [32].

Following the work of Weick *et al.* [28] and Lamowski *et al.* [17], we expand the plasmonic and photonic dynamical variables into creation and annihilation operators defined in reciprocal space for a periodic arrangement of particles. We obtain the Hamiltonian for the plasmon-plasmon interaction as

$$\mathcal{H}_{\mathrm{plpl}} = \sum_{\vec{q},\nu,\nu'} \hbar\sqrt{\Lambda_{\bar{\nu}}\Lambda_{\bar{\nu}'}}S_{\nu,\nu'}^{\bar{\nu},\bar{\nu}'}(\vec{q})(b_{-\vec{q},\nu}^\dagger + b_{\vec{q},\nu})$$
$$\times (b_{\vec{q}',\nu'}^\dagger + b_{-\vec{q}',\nu'}), \quad (19)$$

where $b_{\vec{R},\nu} = 1/\sqrt{N_{\mathrm{cells}}}\sum_{\vec{q}} b_{\vec{q},\nu}\exp(i\vec{q}\cdot\vec{R})$ is the annihilation operator for multipole oscillations of the nanoparticle in the unit cell defined by the lattice vector $\vec{R}$. $\bar{\nu} = D$ for $\nu = 1$–3 which correspond to dipole modes while $\bar{\nu} = Q$ for the $\nu = 4$–8 quadrupole modes. N_{cells} is the number of unit cells. The structure function $S_{\nu,\nu'}^{\bar{\nu},\bar{\nu}'}$ in Eq. (19) depends only on the Bravais lattice; it is given by

$$S_{\nu,\nu'}^{DD}(\vec{q}) = \sum_{\vec{R}} \frac{1}{2}\frac{\delta_{\nu\nu'} - 3(\hat{e}_\nu\cdot\vec{n})(\hat{e}_{\nu'}\cdot\vec{n})}{(R/\bar{R})^3}\exp(i\vec{q}\cdot\vec{R}), \quad (20)$$

when both ν and ν' correspond to dipole modes,

$$S_{\nu,\nu'}^{QQ}(\vec{q}) = \sum_{\vec{R}} \frac{1}{6}\left\{35\frac{(\chi_\nu:\hat{n}\hat{n})(\chi_{\nu'}:\hat{n}\hat{n})}{(R/\bar{R})^5}\right.$$
$$\left. - 20\frac{(\chi_\nu\chi_{\nu'}:\hat{n}\hat{n})}{(R/\bar{R})^5} + 2\frac{(\chi_\nu:\chi_{\nu'})}{(R/\bar{R})^5}\right\}\exp(i\vec{q}\cdot\vec{R}), \quad (21)$$

when both ν and ν' correspond to quadrupole modes, and

$$S_{\nu,\nu'}^{DQ}(\vec{q}) = \sum_{\vec{R}} \frac{1}{2}\left[-5\left(\chi_{\nu'}:\frac{\hat{n}\hat{n}}{(R/\bar{R})^4}\right)(\hat{n}\cdot\hat{e}_\nu)\right.$$
$$\left. + 2\left(\chi_{\nu'}:\frac{\hat{n}\hat{e}_\nu}{(R/\bar{R})^4}\right)\right]\exp(i\vec{q}\cdot\vec{R}), \quad (22)$$

when ν corresponds to a dipole mode and ν' corresponds to a quadrupole mode. Here, $\hat{a}\hat{b}$ corresponds to dyadics formed by the two unit vectors $\hat{a}$ and $\hat{b}$. Also, $\hat{n} = \vec{R}/R$ and $\bar{R} = (V_{\mathrm{uc}})^{1/3}$, with V_{uc} being the volume of the unit cell. The dipole-dipole interaction does not converge for $q \to 0$ in a filled three-dimensional space [17,37]. For wave vectors below a cutoff value q_c, i.e., $|q| < |q_c|$, the dipole-dipole structure function S^{DD} is replaced by $S_{\nu,\nu'}^{DD} = -2\pi[\delta_{\nu\nu'} - (\hat{e}_\nu\cdot\hat{q})(\hat{e}_{\nu'}\cdot\hat{q})]/3$. The value of q_c that allows for a smooth dispersion relation depends on the Bravais lattice and on the number of unit cells considered. The plasmon-plasmon interaction Hamiltonian in Eq. (19) contains coupling factors $\Lambda_{\bar{\nu}}$; they are given by

$$\Lambda_D = \frac{\mathrm{Q}_D^2}{8\pi\epsilon_0\epsilon_m M\omega_D V_{\mathrm{uc}}} \quad (23)$$

and

$$\Lambda_Q = \frac{(\mathrm{Q}_Q\bar{\rho})^2}{8\pi\epsilon_0\epsilon_m M\omega_Q V_{\mathrm{uc}}^{5/3}}, \quad (24)$$

where ϵ_m is the dielectric constant of the surrounding medium, which is assumed to be a positive constant.

We now turn to the interaction between plasmons and photons. The first-order part of the plasmon-photon coupling can be written as

$$\mathcal{H}_{\mathrm{plpt}}^{(1)} = i\hbar\sum_{\vec{q},\vec{G},\lambda,\nu} \omega_{\bar{\nu}}\xi_{\lambda,\vec{G}}^\nu (b_{-\vec{q},\nu}^\dagger - b_{\vec{q},\nu})(c_{-\vec{q}-\vec{G},\lambda} + c_{\vec{q}+\vec{G},\lambda}^\dagger),$$
$$(25)$$

where $\vec{G}$ runs through the reciprocal lattice vectors for the chosen lattice and is responsible for the Umklapp effects ($\vec{G} \neq 0$). We defined

$$\xi_{\lambda,\vec{G}}^\nu(\vec{q}) = \mathrm{f}_D(|\vec{q}+\vec{G}|)\xi_0^D(\vec{q})P_{\nu,\lambda}^D(\vec{q}+\vec{G}) \quad (26)$$

for $\bar{\nu} = D$, and

$$\xi_{\lambda,\vec{G}}^\nu(\vec{q}) = i\mathrm{f}_Q(|\vec{q}+\vec{G}|)|\vec{q}+\vec{G}|\bar{R}\xi_0^Q(\vec{q})P_{\nu,\lambda}^Q(\vec{q}+\vec{G}) \quad (27)$$

for $\bar{\nu} = Q$, where

$$\xi_0^{\bar{\nu}}(\vec{q}) = \sqrt{\frac{2\pi\Lambda_{\bar{\nu}}}{\omega_{pt}(\vec{q})}} \quad (28)$$

and

$$P_{\nu,\lambda}^D(\vec{q}) = \hat{e}_\nu\cdot\hat{e}_\lambda$$
$$P_{\nu,\lambda}^Q(\vec{q}) = \tfrac{1}{2}[\chi_\nu:\hat{e}_q\hat{e}_\lambda + \hat{e}_\lambda\hat{e}_q], \quad (29)$$

with $\hat{e}_\lambda$ being functions of $\vec{q}$, since for both values of λ the vector potential is perpendicular to the wave vector $\vec{q}$.

Finally, the second-order part of the plasmon-photon interaction is

$$\mathcal{H}^{(2)}_{\text{plpt}} = \hbar \sum_{\vec{q},\lambda,\lambda',\vec{G},\vec{G}'} \Xi^{\lambda\lambda'}_{\vec{G},\vec{G}'}(\vec{q})(c^{\dagger}_{-\vec{q}-\vec{G}',\lambda'} + c_{\vec{q}+\vec{G}',\lambda'})$$
$$\times (c_{-\vec{q}-\vec{G},\lambda} + c^{\dagger}_{\vec{q}+\vec{G},\lambda}), \qquad (30)$$

where

$$\Xi^{\lambda\lambda'}_{\vec{G},\vec{G}'}(\vec{q}) = \sum_{\nu} \omega_{\bar{\nu}} \xi^{\nu*}_{\lambda'\vec{G}'}(\vec{q}) \xi^{\nu}_{\lambda\vec{G}}(\vec{q}). \qquad (31)$$

It is interesting to note that for each photon mode the second-order photon coupling is obtained in terms of a sum involving the matrix elements of the first-order interactions. In the weak-coupling regime, this term can be obtained using the Thomas-Reiche-Kuhn (TRK) sum rule and has the important effect of balancing out the first-order term as q goes to zero, thus preventing superradiant phase transitions [38]. Recently, a generalized sum rule was obtained for the strong-coupling regime [39]. It is written in terms of the eigenstates of the full Hamiltonian and cannot be directly applied to simplify our calculations. However, the existence of such a rule indicates that even in the strong-coupling regime, the second-order terms perfectly balance out the first-order interactions as $\vec{q} \to 0$.

We also comment on how Umklapp processes contribute to the plasmon-polariton formation. As the light-plasmon coupling become large, photons with wave vectors beyond the first Brillouin zone effectively couple to the plasmons in the first Brillouin zone through Umklapp effects, although these photons have a much larger energy. In addition, as the system approaches the DSC regime, Umklapp effects contribute to the second-order photon-photon interaction through the $\vec{G} \neq \vec{G}'$ terms in Eq. (30). The second-order term also couples photon modes with different polarizations λ and λ', effectively mixing these two otherwise independent photon states and opening pathways for different types of chiral activity in strongly coupled systems.

To calculate the polaritonic modes, we can follow the work of Xiao [40], and define a Bogoliubov vector operator

$$\Phi_{\vec{q}} = \begin{pmatrix} \bar{b}_{\vec{q}} \\ \bar{c}_{\vec{q}} \\ \bar{b}^{\dagger}_{-\vec{q}} \\ \bar{c}^{\dagger}_{-\vec{q}} \end{pmatrix}, \qquad (32)$$

where $\bar{b}_{\vec{q}}$ and $\bar{b}^{\dagger}_{\vec{q}}$ are column vectors with each entry being an operator corresponding to a different plasmonic mode ν. $\bar{c}_{\vec{q}}$ and $\bar{c}^{\dagger}_{\vec{q}}$ are column vectors with operators for each polarization λ and each reciprocal lattice vector $\vec{G}$ considered. The values of $\vec{q}$ are limited to the positive half of the Brillouin zone. $\Phi_{\vec{q}}$ obeys the following dynamical equation [40],

$$i\hbar \frac{d}{dt} \Phi_{\vec{q}} = D_{\vec{q}} \Phi_{\vec{q}}, \qquad (33)$$

with

$$D_{\vec{q}} = \hbar \begin{pmatrix} \bar{\alpha}_{\vec{q}} & \bar{\gamma}_{\vec{q}} \\ -\bar{\gamma}^{\dagger}_{\vec{q}} & -\bar{\alpha}^{\star}_{\vec{q}} \end{pmatrix}, \qquad (34)$$

where

$$\bar{\alpha}_{\vec{q}} = \begin{pmatrix} \bar{\omega}_{pl} + \bar{\Lambda}(\bar{S}_{\vec{q}} + \bar{S}_{-\vec{q}}) & \bar{\omega}_{pl}\bar{\xi}_{\vec{q}} \\ \bar{\omega}_{pl}\bar{\xi}^{\dagger}_{\vec{q}} & \bar{\omega}^{pt}_{\vec{q}} + 2\bar{\Xi}_{\vec{q}} \end{pmatrix} \qquad (35)$$

and

$$\bar{\gamma}_{\vec{q}} = \begin{pmatrix} \bar{\Lambda}(\bar{S}_{\vec{q}} + \bar{S}_{-\vec{q}}) & \bar{\omega}_{pl}\bar{\xi}_{\vec{q}}(\vec{q}) \\ -\bar{\omega}_{pl}\bar{\xi}^{\dagger}_{\vec{q}} & 2\bar{\Xi}_{\vec{q}} \end{pmatrix}. \qquad (36)$$

Here, $\bar{\omega}_{pl}$ and $\bar{\omega}_{pt}$ are diagonal matrices with the energies of each of the plasmonic modes ν of the metallic nanoparticle and the photon modes (labeled by λ and $\vec{G}$) that are taken into consideration. The matrix $\bar{\Lambda}$ is given by $\bar{\Lambda} = \sqrt{\Lambda_{\nu}\Lambda_{\nu'}}$, $\bar{S}_{\vec{q}}$ is given by Eqs. (20)–(22), $\bar{\xi}_{\vec{q}}$ by Eqs. (26) and (27), and $\bar{\Xi}_{\vec{q}}$ by Eq. (31). A detailed description of these matrices is given in the Supplemental Material.

The dynamical matrix $D_{\vec{q}}$ is diagonalized by a Bogoliubov-Valentin transformation $T^{-1}_{\vec{q}} D_{\vec{q}} T_{\vec{q}}$, which leads to a new set of creation and annihilation operators, $\Psi^{\dagger}_{pp}(\vec{q})$ and $\Psi_{pp}(\vec{q})$, given by $\Psi_{pp}(\vec{q}) = T_{\vec{q}} \Phi_{\vec{q}}$ with eigenvalues $\hbar\omega_{pp}(\vec{q})$ [40]. These operators correspond to the creation and annihilation of mixed excitations called plasmon polaritons which have properties of both plasmons and photons [17]. The eigenvalues can be associated with the plasmon-polariton dispersion. It should be mentioned that the transformation matrices $T_{\vec{q}}$ mix terms with both creation and annihilation operators of plasmons and photons, giving rise to many of the phenomena expected in the extreme regimes of light-matter coupling [22,23,25,26].

B. Quasistatic approximation

In this section we discuss the input parameters of our microscopic model. We want to calculate the plasmon-polariton dispersions of plasmonic supercrystals and compare them to experimental results as well as calculations performed with other techniques. To do so, we need the frequencies of the dipole ω_D and quadrupole ω_Q plasmon resonances in metallic nanoparticles as well as their coupling factors Λ_D and Λ_Q.

The dipole and quadrupole frequencies are obtained within the quasistatic approximation. We consider a Drude metal with permittivity $\epsilon(\omega) = \epsilon_d - (\omega_p/\omega)^2$, neglecting losses. ω_p is the plasma frequency of the metal and ϵ_d a dielectric constant that accounts for the screening by bound charges [15]. This yields the frequencies [41,42]

$$\omega_D = \frac{\omega_p}{\sqrt{\epsilon_d + 2\epsilon_m}} \qquad (37)$$

and

$$\omega_Q = \frac{\omega_p}{\sqrt{\epsilon_d + (3/2)\epsilon_m}}. \qquad (38)$$

The coupling parameters are obtained by considering the screened effective charges,

$$Q_l = \frac{(2l+1)\epsilon_m}{l\epsilon(\omega) + (l+1)\epsilon_m} Q^0_l, \qquad (39)$$

where $l = 1$ for dipole and $l = 2$ for quadrupole modes [43]. This leads to

$$\Lambda_D = \frac{9\epsilon_m \omega_D}{8\pi(\epsilon_d + 2\epsilon_m)} F \qquad (40)$$

and

$$\Lambda_Q = \left(\frac{3}{4\pi}\right)^{5/3} \frac{5\epsilon_m \omega_Q}{12[\epsilon_d + (3/2)\epsilon_m]} F^{5/3}, \qquad (41)$$

where $F = 4\pi\rho^3/3V_{uc}$ is the metal fill fraction, i.e., the fraction of the unit cell volume that is filled by metal. The expressions for Λ_D and Λ_Q allow a first estimate of the importance of the dipole and quadrupole contributions to the plasmon-polariton dispersion and light-matter coupling. The quasistatic approximation is valid for small particles as the dipole and quadrupole plasmon frequencies start to decrease with increasing nanoparticle radius, and the relative contributions of the higher-order multipoles to scattering and absorption become more relevant. The approximation applies for gold and silver nanoparticles up to $\rho \sim 50$ nm [41]. For larger particles, the plasmon frequencies and effective charges must be calculated using a more detailed model or be taken as fitting parameters to the model and the contribution from higher-order multipoles should be considered [44].

Within this quasistatic approximation, the ratio between the quadrupole and dipole coupling factors,

$$\frac{\Lambda_Q}{\Lambda_D} = \frac{5}{18}\left(\frac{3}{4\pi}\right)^{2/3}\left(\frac{\epsilon_d + 2\epsilon_m}{\epsilon_d + (3/2)\epsilon_m}\right)^{3/2} F^{2/3}, \qquad (42)$$

scales with $F^{2/3}$. The prefactor ranges from ~ 0.10 for $\epsilon_d \gg \epsilon_m$ to ~ 0.16 for $\epsilon_m \gg \epsilon_d$. In simple crystals (Bravais lattices) of spherical nanoparticles $F \leqslant 0.74$, with the largest packing density for fcc and hcp lattices. The quadrupole-quadrupole (QQ) interaction is in this case limited to about 13% of the dipole-dipole (DD) interaction and the dipole-quadrupole (DQ) interaction to 36%. Especially for smaller packing fractions the dipole-derived terms are expected to dominate the polariton dispersion, but we expect important contributions of the quadrupole terms for high packing. Even larger metal fill fractions may be obtained with nonspherical nanoparticles and in supercrystals with more than one nanoparticle per unit cell [1,5]. The QQ and DQ coupling terms are much weaker than the DD interaction. Even for large filling, we expect the dipole and quadrupole excitations of the nanoparticles to dominate the supercrystal optical response. Higher-order multipoles will not strongly affect the results obtained with this model even as filling reaches its maximum (gapless supercrystals). The main limitation of our model with increasing the filling factor stems from the fact that we neglect the charge exchange between the particles. Our model is therefore limited to interparticle gaps on the order of 1 nm, depending on the dielectric properties of the surrounding medium [45].

The Rabi frequency associated to the interaction of light with the dipole and quadrupole plasmons can be estimated as $\Omega_R^\nu = \omega_{\bar{\nu}} \xi_0^\nu (\omega_{\bar{\nu}}/c)$, where $\bar{\nu} = D, Q$ for dipoles and quadrupoles, respectively. Within the quasistatic approximation we obtain the explicit expressions

$$\Omega_R^D = \omega_D \sqrt{\frac{3F_0}{4}\left(\frac{3\epsilon_m}{\epsilon_d + 2\epsilon_m}\right)} f^{1/2} \qquad (43)$$

and

$$\Omega_R^Q = \omega_Q \sqrt{\frac{\pi}{3}\left(\frac{3F_0}{4\pi}\right)^{5/3}\left(\frac{5\epsilon_m}{2\epsilon_d + 3\epsilon_m}\right)} f^{5/6}, \qquad (44)$$

where we define the fill factor $f = F/F_0$ and F_0 is the maximum fill fraction for a given lattice. For an fcc supercrystal the Rabi frequencies are limited to $\Omega_R^D = 0.91\omega_D$ and $\Omega_R^Q = 0.31\omega_Q$, which is obtained by setting $\epsilon_m \gg \epsilon_d$, $f = 1$, and $F_0 = 0.74$ in Eqs. (43) and (44). This places the Rabi frequencies on the order of eV for high packing densities, in excellent agreement with our recent experimental results [6].

C. Validating the model

Before discussing and analyzing the band structure and properties of plasmon polaritons, we demonstrate the validity of our model by comparing it to FDTD simulations. We first describe the parameters used in both simulations. We considered an fcc nanoparticle crystal and the high-symmetry ΓL and ΓK directions. The nanoparticle diameters were $d = 50$ nm with an interparticle (center to center) distance of $a = 65$ nm, which yields a metal fill factor $f = 0.46$. The calculations were done with the Drude model using a plasma frequency $\hbar\omega_p = 9$ eV and $\epsilon_d = 1$. The nanoparticles were placed in vacuum ($\epsilon_m = 1$). According to the quasistatic approximation, the dipole plasmon of the isolated nanoparticle has energy $\hbar\omega_D = 9/\sqrt{3} \sim 5.19$ eV and the quadrupole plasmon is at $\hbar\omega_Q \sim 5.69$ eV. We note that this choice of parameters places the nanoparticle dipole plasmon at about the middle of the energy range spanned by the photons within the first Brillouin zone of the crystal. We argue that this is an appropriate condition to verify the validity of the model. Real metallic nanoparticles will have different plasma frequencies and effective dielectric constants that lead to lower dipole and quadrupole plasmon energies. Therefore, the lattice parameters for which the above condition is fulfilled will depend on the choice of nanoparticle supercrystal. For instance, for gold nanoparticles, the dipole plasmon energy is ~ 2.3 eV. An average photon energy of ~ 2.3 eV requires a gold nanoparticle supercrystal with a lattice constant ~ 150 nm. We should also stress that the dipole and quadrupole coupling constants depend on the effective dielectric constants ϵ_d and ϵ_m.

For the microscopic quantum calculation we considered Umklapp processes with $\vec{G}$ within up to six Brillouin zones. Plasmon-polariton energy differences of up to 10% were obtained for some of the modes if Umklapp processes were neglected (see Fig. S1 for details). The lattice vector summation in real space for calculating S^{DD} was performed for $|\vec{R}|$ below a cutoff radius $R_D = 60\bar{R}$. For S^{DQ} and S^{QQ} a cutoff radius of $R_Q = 7\bar{R}$ sufficed to achieve full convergence. This reflects the fact that the dipole-quadrupole and quadrupole-quadrupole interactions fall off faster with distance than dipole-dipole coupling. A cutoff wave vector $q_c = 0.3\pi/a$ was used for the lattice sums. These parameters were used throughout the paper, unless otherwise stated.

The FDTD simulations were done with the commercial software package Lumerical FDTD Solutions. We constructed the unit cell of an fcc crystal that is composed of spherical nanoparticles. The simulation geometry is described in detail in the Supplemental Material, Fig. S2 [32]. The nanoparticles were assigned the dielectric function $\epsilon(\omega) = \epsilon_d - \omega_p^2/(\omega^2 - i\gamma\omega)$ with a loss rate $\hbar\gamma = 65$ meV (see above for the other parameters). We used a mesh size of 1 nm to discretize space. To calculate the polariton dispersion we used local emitters
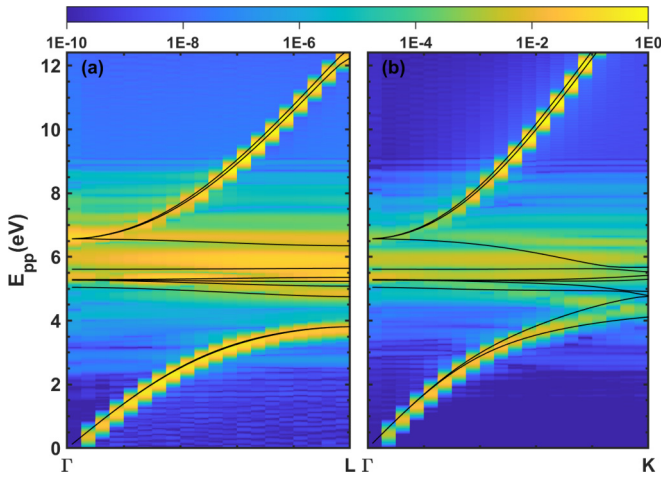
FIG. 1. Polariton band structure of an fcc crystal of spherical nanoparticles along the (a) ΓL and (b) ΓK high-symmetry directions. Solid lines were calculated with the microscopic quantum model. The color map shows the magnitude (in log scale) of the normalized electric field obtained from FDTD simulations as a function of energy and momentum. $\hbar\omega_p = 9$ eV, $\epsilon_m = \epsilon_d = 1$, $a = 65$ nm, and $f = 0.46$.

and point monitors inside the crystal [46]. The point dipoles radiated light along the [111] (ΓL) or [110] (ΓK) direction. To avoid artifacts from the discretized boundaries of the nanoparticles we placed the point dipoles and monitors at a single lattice site that was far away from the metal (see Fig. S2). A 0.7 fs light pulse was injected and the electric field recorded in the time interval from 10 to 50 fs by the point monitor. To avoid the detection of the electric field from the light sources we excluded the time interval from 0 to 10 fs with a Gaussian apodization filter. The frequency-dependent electric field was then obtained by a Fourier transformation. We used Bloch periodic boundary conditions to choose a specific wave vector. By running a sweep of simulations for different wave vectors we obtained the polaritonic band structure.

Figure 1 compares the band structure obtained with FDTD and the microscopic model. The background of the figure is a color map of the integrated intensity of the electric field as a function of ω and q, which corresponds to the polariton dispersion predicted by the FDTD simulations. The black lines show the plasmon-polariton dispersion calculated with the microscopic quantum model. Our model reproduces the FDTD dispersion very well. The far-field response of the supercrystal is dominated by the two dipole-derived bands [6]. These are the bands with the lowest and highest energy in Fig. 1, which are excellently described by the quantum mechanical model. Along the ΓL direction [Fig. 1(a)], the quadrupole bands between the two dipole-derived states agree also between FDTD and the microscopic model. The FDTD simulation appears to contain more states, which originate from hexapole eigenmodes of the nanoparticles or artifacts of the simulation. The ΓK direction [Fig. 1(b)] is the high-symmetry direction of the fcc lattice that is most strongly affected by the quadrupole modes. As discussed below, the dipole-only model strongly overestimates the energy of the lowest lying polariton band near the K point, whereas

the inclusion of the quadrupole modes results in reasonable agreement with the FDTD results.

The two FDTD simulations shown in Fig. 1 took several hours each, whereas the microscopic quantum mechanical band structure was obtained in seconds. Our model allows a rapid screening of many supercrystal structures, fill factors, nanoparticle shapes, and so forth. Its true strength, however, goes beyond its computational capability: The microscopic model allows an in-depth study of the origin of the plasmon-polariton band structure and its properties, as we will show in the following section.

III. RESULTS AND DISCUSSION

We modeled the plasmon-polariton band structure of fcc nanoparticle supercrystals using our microscopic model. With the simulations we can explain the contribution of the interaction between the nanoparticles and with the electromagnetic modes to the final polariton states. We are able to extract the coupling and mixing of dipole- and quadrupole-derived states in this particular Bravais lattice. Finally, we show how to extract the dipolar, quadrupolar, and photonic contribution to each polariton state. The results impressively reproduce the decoupling of light and matter in the USC and DSC regime [6,24].

A. Collective plasmon modes

We model the optical properties of plasmonic nanoparticle supercrystals in a step-by-step approach. We start with the interaction between the dipole and quadrupole states of different nanoparticles that gives rise to collective plasmon modes. This initial plasmonic band structure omits the coupling to electromagnetic states [6,17,28]. Including the photons will later create the supercrystal plasmon polaritons.

In Fig. 2 we show the plasmonic band structure of an fcc crystal considering both dipole and quadrupole nanoparticle excitations. In each panel we also show the band structures for the dipole (blue) and quadrupole (red) modes when turning off the interaction between the dipole and quadrupole states. For the lowest fill factor $f = 0.06$ in Fig. 2(a) the dipole and quadrupole states do not cross and are largely decoupled, as can be seen by the agreement between the black and the blue/red lines. The lowest plasmonic state at the Γ point [$\sim$5.1 eV in Fig. 2(a)] is a twofold degenerate dipole-induced state [17]. It remains degenerate along the ΓX and ΓL directions but splits along ΓK. These two bands are associated with transverse oscillations of the plasmons, i.e., the electrons oscillate perpendicular to the propagation direction. The uppermost dipole-induced band [$\sim$5.4 eV at Γ in Fig. 2(a)] is a longitudinal oscillation that does not couple directly with light.

The quadrupole states are constant across the Brillouin zone for $f = 0.06$, but become dispersive for the larger fill factors $f = 0.31$ [Fig. 2(b)] and 0.90 [Fig. 2(c)]. The quadrupole states consist of five bands that are two- and threefold degenerate at the Γ point [for example, at 5.62 and 5.75 eV in Fig. 2(c)]. Along the ΓL direction the threefold degenerate state splits into a twofold and a nondegenerate band, while the lower branch remains twofold degenerate.
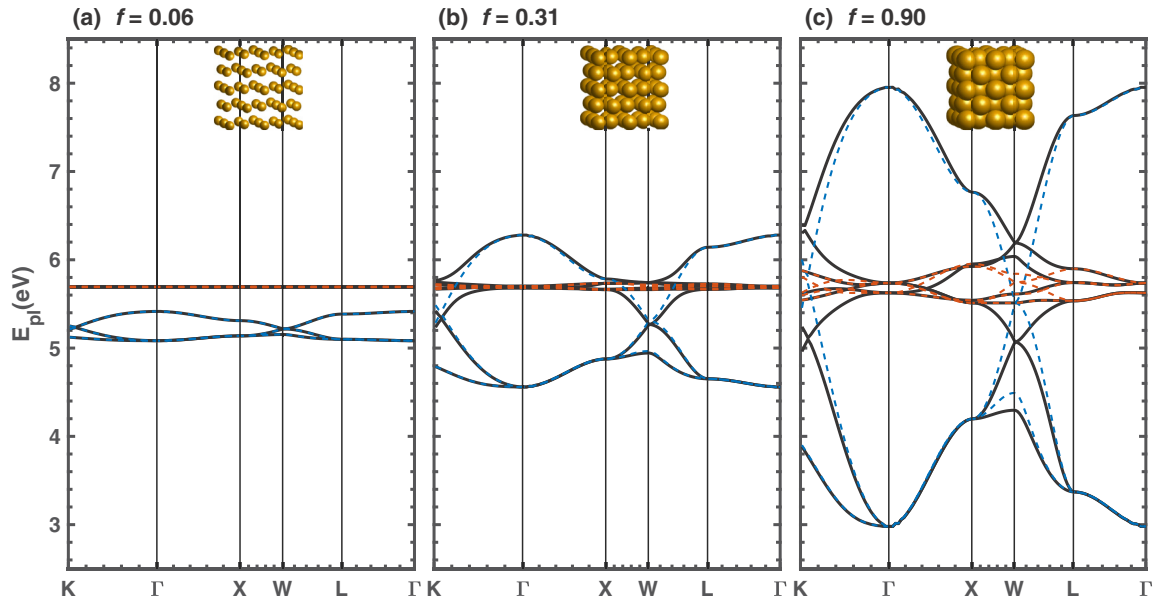
FIG. 2. Collective plasmon dispersion along the high-symmetry directions of an fcc lattice for fill factors (a) $f = 0.06$, (b) 0.31, and (c) 0.90. The blue (red) lines are induced by the dipole (quadrupole) plasmons of the nanoparticles neglecting dipole-quadrupole interactions. The black lines are a full calculation including dipole and quadrupole modes and their interaction. The insets show a sketch of the supercrystal structure for each configuration. $\hbar\omega_p = 9$ eV, $\epsilon_m = \epsilon_d = 1$, and $a = 62$ nm.

Along the high-symmetry lines the bands split and cross, but overall the quadrupole dispersion is much narrower (0.3 eV for $f = 0.9$) than the dispersion of the dipole bands (5 eV for $f = 0.9$). The reason is that the dipole-dipole coupling is much stronger than the quadrupole-quadrupole coupling, with a ratio of $\Lambda_D/\Lambda_Q \sim 13$.

The dispersion of the dipole-derived plasmon band increases rapidly with the metal fill fraction (Fig. 2). For $f > 0.1$ the dipole band crosses the energy of the quadrupole states. The two types of bands overlap and the dipole-quadrupole interaction strongly affects the plasmonic dispersion. The magnitude of this interaction can be qualitatively evaluated by observing the differences between the black lines (including the DQ interaction) and the blue and red lines in Fig. 2. For $f = 0.31$ and 0.90 the differences are very pronounced, especially in the ΓK and the XWL directions. This is in contrast with the results for $f = 0.06$ [Fig. 2(a)], where the black and blue/red lines are identical throughout the Brillouin zone.

The dipole-quadrupole mixing depends on the symmetry of the plasmonic bands. For example, along the ΓL direction the states remain unchanged by the coupling, indicating that dipole and quadrupole modes cannot couple in this high-symmetry direction. This explains why the dipole approximation worked very well for analyzing the optical spectra of gold nanoparticle supercrystals where the light propagated normal to the (111) surface [6] (see the discussion further below). In contrast, DQ coupling is allowed along the ΓK and the XWL high-symmetry lines. The mixing prevents the crossing of the transverse and longitudinal dipole-derived bands at W and close to K (see Fig. 2). Dipole-quadrupole coupling also reduces the splitting of the transverse states. For the ΓK direction, two out of the five quadrupole bands are strongly mixed with the dipole modes, while the other

three remain practically unchanged. We also note that the lowest transverse dipole bands are less affected by the dipole-quadrupole coupling, because of the larger energy difference between the states.

B. Plasmon polaritons

After having examined the bare plasmon bands, we include the coupling to free-space photons and calculate the plasmon-polariton dispersion. The polaritons are coupled electronic and electromagnetic eigenstates of the nanoparticle supercrystals [6,17,31,47]. In experiments with gold nanoparticle supercrystals these excitations determined the optical response for energies below the interband transitions [6]. Figures 3(a)–3(c) show the plasmon-polariton bands obtained by including the plasmon-photon interaction, considering Umklapp processes up to the sixth Brillouin zone ($n_{BZ} = 6$). To allow for a comparison, we also show as dashed lines the bare plasmon (black) and photon (yellow) energies. For the smallest fill factor ($f = 0.06$), the light-matter interaction is determined mainly by the dipole excitations. The coupling of the transverse dipole bands and photons gives rise to a pronounced level anticrossing, resulting in plasmon-polariton bands with a dispersion E_{pp} that is very different from the uncoupled states [6,17,31,47]. We observe two nearly degenerate parabolic bands centered at the Γ point, which we will refer to as the upper plasmon polariton (UPP), and two lower bands, the lower plasmon polaritons (LPPs). The LPPs start off as linear bands with vanishing energy at the Γ point. They bend down and become almost flat at the zone edges. The quadrupole bands remain flat over the entire Brillouin zone in Fig. 3(a), because the interaction with light is negligible at this metal fill fraction. The longitudinal dipole-derived bands do not couple with light and their polariton dispersion remains unchanged compared to the bare plasmons.
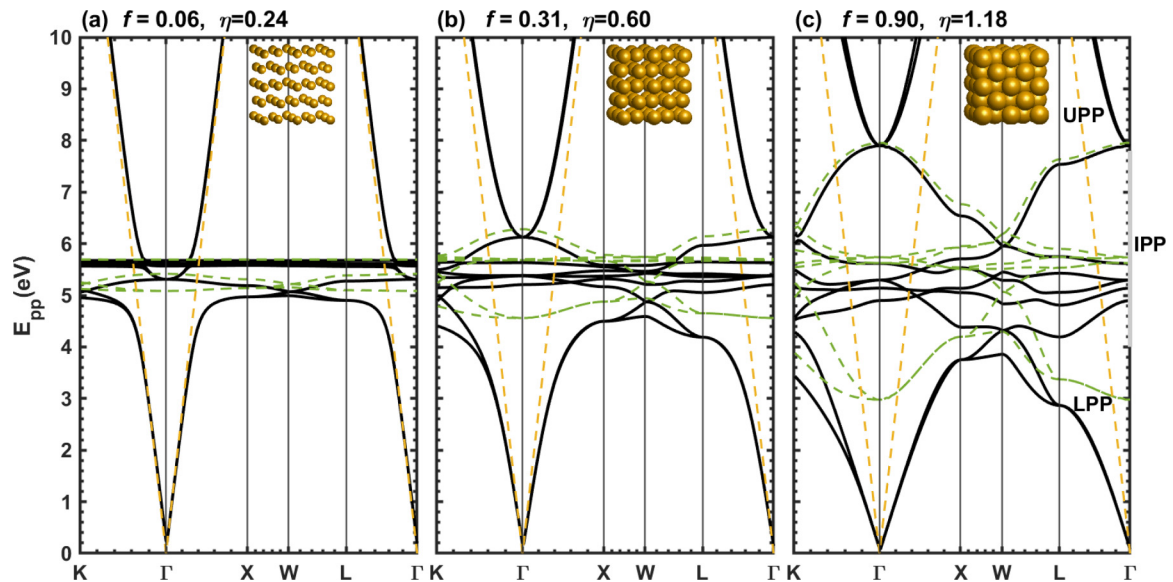
FIG. 3. Plasmon-polariton dispersion along the high-symmetry directions of an fcc crystal with metal fill factors (a) $f = 0.06$, (b) 0.31, and (c) 0.90. Black lines are calculated including all terms and interactions, while green dashed lines show the dispersion of the bare plasmons. Yellow dashed lines show the bare photon dispersion. The insets show a sketch of the supercrystal structure for each configuration. $\hbar\omega_p = 9$ eV, $\epsilon_m = \epsilon_d = 1$, and $a = 62$ nm.

With increasing metal fill factor quadrupole modes mix with the dipole plasmons and the photons, resulting in six intermediate plasmon polaritons (IPPs) [Figs. 3(b) and 3(c)]. This occurs because the coupling between the plasmon and between plasmons and photons increases with metal fill fraction. The topmost IPP band corresponds mainly to the longitudinal dipole-derived band that does not couple directly with light and only weakly with the quadrupole modes. The five other bands are mainly composed of quadrupolelike oscillations which are downshifted by their interaction with the electromagnetic field. This downshift is different for each of the bands, effectively increasing the bandwidth of IPPs. For instance, for $f = 0.90$, the energy difference between the lower and upper quadrupole-derived plasmon polaritons at the X point is $\sim$1.3 eV. This is more than four times larger than the width obtained for the plasmon bands without coupling to photons, 0.3 eV (see the dashed lines).

The UPP and LPP bands in the ΓL direction are derived from the dipole modes without quadrupole mixing, due to the absence of a dipole-quadrupole interaction along this high-symmetry direction. This explains why the polariton band structure observed along the [111] direction of gold nanoparticle supercrystals was excellently described by a single-band Hopfield model and microscopic calculations within the dipole approximation [6]. The situation is different along the ΓK and the XWL directions, for which the dipole-quadrupole coupling is strong, as seen in Fig. 2. Along these directions, the dipole-quadrupole and the light-quadrupole interactions lead to an anticrossing between the quadrupole and dipole bands, thus effectively pushing down the topmost LPP. This result shows that a complete and accurate description of metallic supercrystals requires that quadrupole modes and Umklapp processes (see Supplemental Material) are included in the model [32]. The strong dependence of the coupling on the direction in the Brillouin zone points towards symmetry-

based selection rules for dipole-quadrupole and light-matter coupling, which would be interesting to study for various crystal symmetries.

We now examine the coupling and level anticrossing of the dipole and quadrupole modes and the photons in greater detail. In Fig. 4(a) we show the energies of the bare plasmon and photon bands at $q = 0.17\,\Gamma K$ as a function of the metal fill factor and in Fig. 4(b) the corresponding energies of the plasmon-polariton bands. The colors indicate the magnitude of the contribution of dipole (blue) and quadrupole (red) modes and photons (yellow) to the states according to the color code triangle in Fig. 4(a). Without light-matter coupling, the longitudinal dipole-derived plasmon modes [blue lines in Fig. 4(a)] upshift almost linearly with filling, while the quadrupole energies remain nearly constant. At $f \sim 0.12$, the energies of the two sets of bands cross. For one of the quadrupole modes, the interaction with the longitudinal dipole band causes an avoided crossing with a gap on the order of 0.01 eV [see the enlarged panel in Fig. 4(c)]. The other quadrupole and dipole bands are only weakly affected by the DQ interaction.

Without light-matter coupling the photon energy remains at $E = 2.6$ eV, independent of filling. When light-matter coupling is "turned on," plasmon polaritons form. The UPP band is mainly composed of transverse dipole-derived plasmon states at $0.17\,\Gamma K$ and for vanishing metal content $f \sim 0$. With increasing filling the UPPs become more photon-like (yellow color); at the same time, their energy increases in parallel with the longitudinal dipole mode (blue) that does not interact with light. The LPP shifts to smaller energies with increasing f and obtains a strong dipole plasmon contribution.

The spectral range of the anticrossing of the UPPs and the quadrupole bands is shown at a higher magnification in Fig. 4(d). Along the ΓK direction, dipole
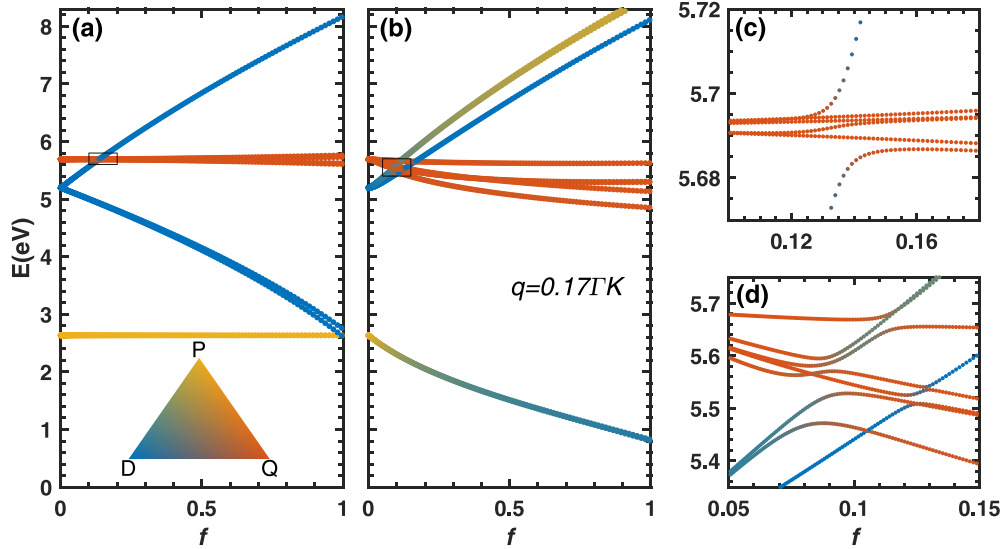
FIG. 4. Energies of (a) the bare plasmon and photon states and of (b) the plasmon-polariton states for $q = 0.17\,\Gamma K$. The coloring indicates the dipole, quadrupole, and photon contribution to each state—see the inset in (a). (c) and (d) show zoomed images of the rectangular areas in (a) and (b), respectively.

plasmons, quadrupole plasmons, and photons all mix into polariton states. As the polarization dependences of the light-quadrupole and light-dipole interactions are different, we expect cross-polarized absorption and chiral activity, which will be studied in a future work. As the fill factor increases further, the UPP bands become increasingly photonlike and their interaction with the quadrupole modes causes the latter to downshift in energy, thus increasing the overall bandwidth of the quadrupole modes.

C. Normalized coupling strength

The normalized coupling strength $\eta = \Omega_R/\omega_0$ compares the Rabi frequency Ω_R to the bare frequency ω_0 of the system. Ω_R can be found from the minimum energy splitting between the LPP and UPP bands (divided by two) and ω_0 from a calculation of the bare plasmon dispersion [21–23]. The normalized coupling strength can be used as a figure of merit for determining whether a given excitation of the system is in the ultrastrong- or deep strong-coupling regimes [22,23]. For $\eta < 0.1$ the system is considered to be in the either the weak- or the strong-coupling regime, depending on the ratio between Ω_R and the losses of the system. For $0.1 < \eta < 1$ the system is in the ultrastrong-coupling regime, while the deep strong coupling is reached for $\eta > 1$. In this section we derive a closed expression for η as a function of our model parameters. It will facilitate choosing a nanoparticle supercrystal for a desired coupling. We will show that a wide range of USC and DSC light-matter interactions can be realized in plasmonic supercrystals.

The bare plasmon energies without coupling to the electromagnetic states depend on the plasmon coupling factors $\Lambda_{\bar{\nu}}$ ($\bar{\nu} = D, Q$) defined in Eqs. (40) and (41). The energies are well described by [6]

$$E_{pl,\nu}(\vec{q}) = \hbar\omega_{\bar{\nu}}\sqrt{1 + s_{\nu,f}(q)\Lambda_{\bar{\nu}}}, \qquad (45)$$

where $s_{\nu,f}(q)$ incorporates the effects of the lattice; it depends only weakly on f. $s_{\nu,f}(q)$ measures the enhancement of the effective plasmon-plasmon coupling due to the crystalline structure. This value can be calculated numerically for each of the plasmon bands at any given q [5]. However, as we are interested in an effective expression, we use a different approach and fit the energy of the lowest lying D and Q bands at the Γ and X points, respectively. These are the wave vectors of the largest bandwidths of the dipole- and quadrupole-derived bands, which give us an overall measure for plasmon-plasmon coupling. Figure 5(a) shows the energies of the upper and lower dipole and quadrupole bands at the Γ and X point. These are fitted to Eq. (45) and the fitting parameters are shown in Table I.
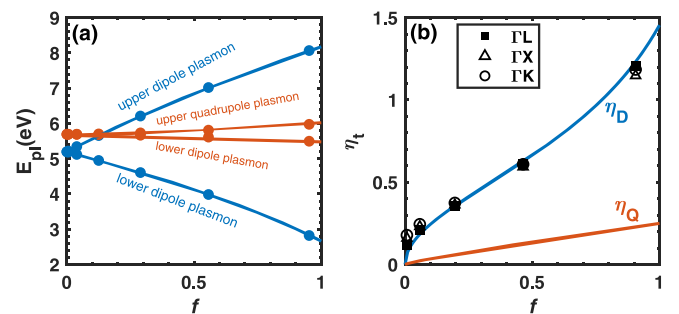
FIG. 5. (a) Energies of the upper and lower dipole (blue symbols) and quadrupole (red symbols) plasmon bands for different values of f of an fcc crystal. The dipole (quadrupole) energies are evaluated at the Γ (X) point. Red and blue lines are fits to the data points, using Eq. (45) (see Table I). (b) Normalized coupling strength η_t of the transverse dipole-derived plasmon band for the ΓL (squares), ΓX (triangles), and ΓK (dots) high-symmetry directions. Blue and red lines are coupling strengths predicted with Eq. (46) for the dipole and quadrupole modes, respectively.

TABLE I. Fit parameters for the upper and lower dipole and quadrupolar states at $q = \Gamma$ and X, respectively. Calculated results were fitted to Eq. (46) with $s_\nu^{u,l}$ as a free parameter.

	Label	q	Value
Upper dipole	s_D^u	Γ	16.5
Lower dipole	s_D^l	Γ	−8.3
Upper quadrupole	s_Q^u	X	14
Lower quadrupole	s_Q^l	X	−7

We now use the Rabi frequencies and dipole and quadrupole coupling strengths in Eqs. (43) and (44) and combine them with the plasmon energy in Eq. (46). We find a compact expression for the maximum reduced coupling

$$\eta_\nu = \sqrt{\frac{2\pi\,\Lambda_{\bar{\nu}}}{\left(1 + \bar{s}_\nu^l \Lambda_{\bar{\nu}}\right)}}, \qquad (46)$$

where s_ν^l are the fitting parameters for the lowest-energy dipole and quadrupole bands at the chosen points (see Table I). For a single plasmonic state η can be found from Eq. (46). A more general expression is necessary for mixed dipole and quadrupole bands. As we are mainly interested in the maximum normalized coupling strength, we will focus on the coupling to the lowest-energy dipole- and quadrupole-derived bands. The solid lines in Fig. 5(b) show the dependence of the reduced dipole and quadrupole coupling in Eq. (46) on the fill factor. The symbols are the reduced coupling strengths of the transverse dipole-derived bands $\eta_t = \Delta E_{\mathrm{UL}}/(2E_{pl,D}^t)$ from a microscopic quantum calculation evaluated at the crossing $|q_0| \sim E_{pl,D}^t/\hbar c$ of the bare dipole plasmon and the photon dispersion along ΓL, ΓX, and ΓK. $E_{pl,D}^t$ is the energy of the transverse dipole-induced plasmon and $\Delta E_{\mathrm{UL}} \sim E_{\mathrm{UPP}}(q_0) - E_{\mathrm{LPP}}(q_0)$ is the energy difference between the upper and lower plasmon polariton branches. The normalized coupling strengths obtained for the different directions correspond well with the value obtained by the expression for the dipole coupling strength $\eta \sim \eta_D$. The fact that this is true even for the ΓK direction indicates that the quadrupole contribution to the coupling strength of the transverse dipole is negligible. Furthermore, it shows that Eq. (46), with the parameters in Table I, can be used to estimate the maximum coupling strength in fcc supercrystals. With this, for a metal fill factor of 3%, the maximum coupling strength is on the order of $\eta = 0.13$, and therefore already in the USC regime ($\eta > 0.1$), while the DSC regime is reached for fill factors above 80% [Fig. 5(b)].

D. Decoupling of light and matter in the USC and DSC regimes

A fascinating signature of ultrastrong and deep strong coupling is the decoupling of light and matter in space and in frequency that leads to a breakdown of the Purcell effect [24]. The Purcell effect describes the increase in radiative damping with increasing light-matter coupling [48]. In the weak- and strong-coupling regimes ($\eta \ll 1$) the radiative damping scales with η^2. De Liberato [24] predicted that the Purcell effect saturates around $\eta \sim 0.5$ and radiative damping de-

creases for higher values of η. Mueller et al. [6] demonstrated the breakdown of the Purcell effect in plasmonic supercrystals for $\eta > 1$. Although this breakdown can be described classically [24], the microscopic quantum description of the plasmon polaritons allows us to directly observe the decoupling with increasing fill fraction, i.e., increasing light-matter coupling.

We use the transformation matrix $T_{\vec{q}}$ introduced in Sec. II A to decompose the plasmon-polariton states into the bare dipole and quadrupole plasmonic and the photonic components. In Fig. 6 we show the plasmon-polariton states decomposed into dipole plasmons, quadrupole plasmons, and photons for three fill factors. For small filling $f = 0.06$ the plasmonic characters are mainly localized in the energy regions of the dipole and quadrupole plasmon bands. The bands with linear dispersion are photonic in character. There is no mixing between the dipole and quadrupole states as expected from our discussion of the bare plasmon dispersion. The dipole plasmon and the photon mix slightly at their crossing, so that the linear bands show a small dipole-plasmon character while the flat band at about 5.19 eV shows a weak photonic character.

With increasing f the mixing between the three states becomes more apparent. For $f = 0.31$ the dipole plasmonic character of the linearly dispersive bands is very pronounced. We also see a non-negligible mixing between the dipole and quadrupole states as well as the quadrupole modes and photons. Peaks related to quadrupole modes should start to appear in the absorption spectra and affect the overall dispersion of the polaritons. The top plasmon-polariton bands acquire a finite mass, because they are composed of photons, dipole plasmons, and even a small contribution from quadrupole modes. Finally, the distribution of the plasmon and photon states becomes asymmetric for lower and upper polaritons: While the low-energy states have a stronger plasmonic component, the upper polaritons are photonic in character.

For the high metal fill factor $f = 0.9$, the linear bands starting at zero energy are almost entirely composed of dipole states, having only weak photonic and quadrupole plasmonic character. The weakly dispersive bands in the gap between UPP and LPP remain strongly plasmonic in nature and are predominantly composed of quadrupole modes, but the states become mixed with photons and with dipole plasmons. This indicates that they should be accessible optically. The UPP branches developed into a pair of massive bands mainly composed of photons. Overall, it is striking that there is little overlap between the three different types of quasiparticles, which is a manifestation of the light-matter decoupling in the DSC regime [6,24]. Indeed, the distribution of states for highest filling resembles the low-filling case: Each component—dipole, quadrupole, and photon—is concentrated in a portion of the polariton dispersion with little contribution to the other states.

The quantum model proposed here gives insight into the nature of the plasmon-polariton states in addition to its excellent description of the plasmon-polariton band structure. In the future, it may be applied to calculate quantum-related properties such as the squeezing of plasmons and photons, the population of the supercrystal ground state with photons and plasmons, and correlation functions of the bare excitations [22,23,25,26,49].
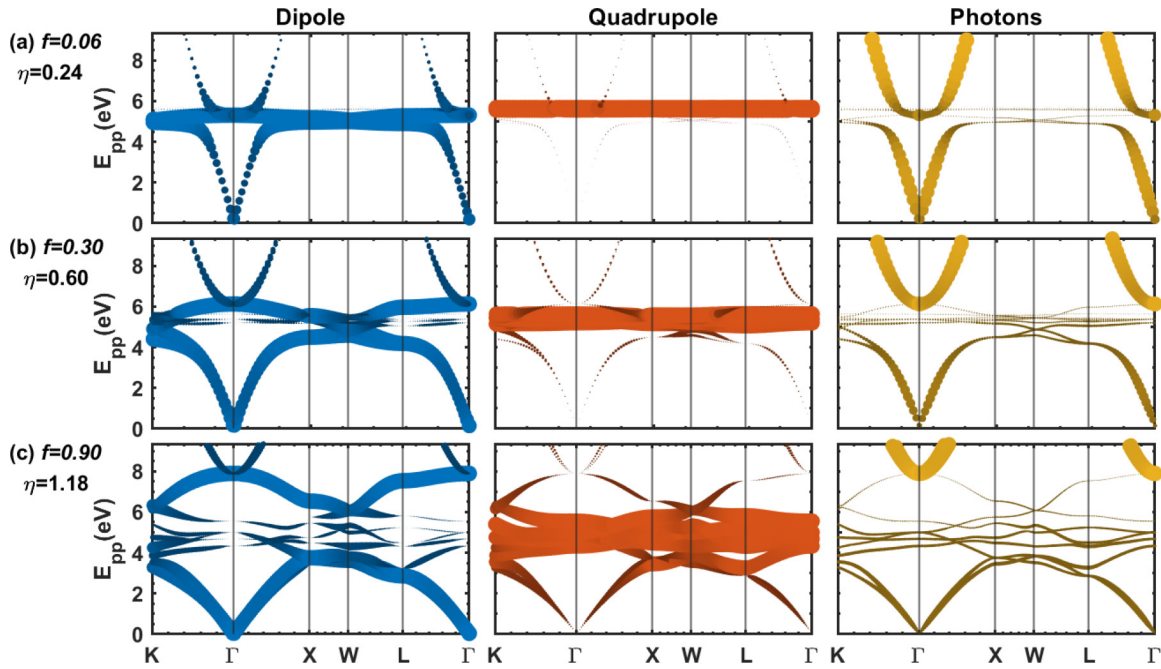
FIG. 6. Decomposition of the plasmon-polariton bands into their dipole (blue), quadrupole (red), and photon (yellow) contributions for fill factors (a) $f = 0.06$, (b) 0.31, and (c) 0.90. The size of the data points shows the magnitude of the relative contributions of each of these bare excitations to the plasmon-polariton bands.

IV. CONCLUSIONS

In conclusion, we proposed a microscopic model to calculate plasmon polaritons in nanoparticle supercrystals. Our model includes the dipole and quadrupole modes of the nanoparticle building blocks and their coupling to photons. We show that the mixing of the dipole and quadrupole-derived states is important for calculating the collective plasmon and plasmon-polariton sates. The microscopic quantum model leads to a closed expression for the reduced light-matter coupling strength of the dipole and quadrupole modes. The dipole-derived states of fcc nanoparticle supercrystals are in the ultrastrong-coupling regime for all realistic fill factors and enter deep strong coupling for fill factors larger than 0.8 (assuming vacuum between the nanoparticles in the crystal). The quantum-based calculations give insight into the unique properties of strongly coupled systems as we show for the example of light-matter decoupling in the DSC regime. The model can be applied for different lattice structures including lattices with more than one particle in the basis. It will contribute to the study and optimization of the many supercrystal structures currently being developed.

[1] M. J. Murray and J. V. Sanders, Close-packed structures of spheres of two different sizes II. The packing densities of likely arrangements, Philos. Mag. A **42**, 721 (1980).

[2] M. A. Boles, M. Engel, and D. V. Talapin, Self-assembly of colloidal nanocrystals: From intricate structures to functional materials, Chem. Rev. **116**, 11220 (2016).

[3] C. B. Murray, C. R. Kagan, and M. G. Bawendi, Synthesis and characterization of monodisperse nanocrystals and close-packed nanocrystal assemblies, Annu. Rev. Mater. Sci. **30**, 545 (2000).

[4] E. V. Shevchenko, T. V. Talapin, C. B. Murray, and S. O'Brien, Structural characterization of self-assembled multifunctional binary nanoparticle superlattices, J. Am. Chem. Soc. **128**, 3620 (2006).

[5] I. Coropceanu, M. A. Boles, and D. V. Talapin, Systematic mapping of binary nanocrystal superlattices: The role of topology in phase selection, J. Am. Chem. Soc. **141**, 5728 (2005).

[6] N. S. Mueller, Y. Okamura, B. G. M. Vieira, S. Juergensen, H. Lange, E. B. Barros, F. Schulz, and S. Reich, Deep strong light-matter coupling in plasmonic nanoparticle crystals, Nature (London) **583**, 780 (2020).

[7] F. Schulz, O. Pavelka, F. Lehmkühler, F. Westermeier, Y. Okamura, N. S. Mueller, S. Reich, and H. Lange, Structural order in plasmonic superlattices, Nat. Commun. **11**, 3821 (2020).

[8] S. Vovk, N. Yazdani, and V. Wood, Manipulating electronic structure from the bottom-up: Colloidal nanocrystal-based semiconductors, J. Phys. Chem. Lett. **11**, 9255 (2011).

[9] A. S. Baimuratov, I. D. Rukhlenko, V. K. Turkov, A. V. Baranov, and A. V. Fedorov, Quantum-dot supercrystals for future nanophotonics, Sci. Rep. **3**, 1727 (2013).

[10] N. S. Mueller, E. Pfitzner, Y. Okamura, G. Gordeev, P. Kusch, H. Lange, J. Heberle, F. Schulz, and S. Reich, Surface-enhanced Raman scattering and surface-enhanced infrared absorption by plasmon polaritons in three-dimensional nanoparticle super-crystals, ACS Nano **15**, 5523 (2021).

[11] D. García-Lojo, S. Núñez-Sánchez, S. Gómez-Graña, M. Grzelczak, I. Pastoriza-Santos, J. Pérez-Juste, and L. M. Liz-Marzán, Plasmonic supercrystals, Acc. Chem. Res. **52**, 1855 (2019).

[12] M. Blanco-Formoso, N. Pazos-Perez, and R. A. Alvarez-Puebla, Fabrication of plasmonic supercrystals and their SERS enhancing properties, ACS Omega **5**, 25485 (2020).

[13] U. Kreibig and M. Vollmer, *Optical Properties of Metal Clusters*, Springer Series in Materials Science Vol. 25 (Springer, Berlin, 1995).

[14] K. Lance Kelly, E. Coronado, L. L. Zhao, and G. C. Schatz, The optical properties of metal nanoparticles: The influence of size, shape, and dielectric environment, J. Phys. Chem. B **107**, 668 (2003).

[15] S. A. Maier, *Plasmonics: Fundamentals and Applications* (Springer, New York, 2007).

[16] N. Meinzer, W. L. Barnes, and I. R. Hooper, Plasmonic meta-atoms and metasurfaces, Nat. Photonics **8**, 889 (2014).

[17] S. Lamowski, C. R. Mann, F. Hellbach, E. Mariani, G. Weick, and F. Pauly, Plasmon polaritons in cubic lattices of spherical metallic nanoparticles, Phys. Rev. B **97**, 125409 (2018).

[18] W. L. Barnes, A. Dereux, and T. W. Ebbesen, Surface plasmon subwavelength optics, Nature (London) **424**, 824 (2003).

[19] V. M. Shalaev, Transforming light, Science **322**, 384 (2008).

[20] M. S. Tame, K. R. McEnery, Ş. K. Özdemir, J. Lee, S. A. Maier, and M. S. Kim, Quantum plasmonics, Nat. Phys. **9**, 329 (2013).

[21] D. G. Baranov, B. Munkhbat, E. Zhukova, A. Bisht, A. Canales, B. Rousseaux, G. Johansson, T. J. Antosiewicz, and T. Shegai, Ultrastrong coupling between nanoparticle plasmons and cavity photons at ambient conditions, Nat. Commun. **11**, 2715 (2020).

[22] A. F. Kockum, A. Miranowicz, S. De Liberato, S. Savasta, and F. Nori, Ultrastrong coupling between light and matter, Nat. Rev. Phys. **1**, 19 (2019).

[23] P. Forn-Díaz, L. Lamata, E. Rico, J. Kono, and E. Solano, Ultrastrong coupling regimes of light-matter interaction, Rev. Mod. Phys. **91**, 025005 (2019).

[24] S. De Liberato, Light-Matter Decoupling in the Deep Strong Coupling Regime: The Breakdown of the Purcell Effect, Phys. Rev. Lett. **112**, 016401 (2014).

[25] M. Artoni, Quantum-optical properties of polariton waves, Phys. Rev. B **44**, 3736 (1991).

[26] M. Cirio, S. De Liberato, N. Lambert, and F. Nori, Ground State Electroluminescence, Phys. Rev. Lett. **116**, 113601 (2016).

[27] J. J. Hopfield, Theory of the contribution of excitons to the complex dielectric constant of crystals, Phys. Rev. **112**, 1555 (1958).

[28] G. Weick and E. Mariani, Tunable plasmon polaritons in arrays of interacting metallic nanoparticles, Eur. Phys. J. B **88**, 7 (2015).

[29] E. C. Le Ru and P. G. Etchegoin, *Principles of Surface-Enhanced Raman Spectroscopy* (Elsevier, Amsterdam, 2009).

[30] S. Reich, N. S. Mueller, and M. Bubula, Selection rules for structured light in nanooligomers and other nanosystems, ACS Photonics **7**, 1537 (2020).

[31] J. Li, G. Sun, and C. T. Chan, Optical properties of photonic crystals composed of metal-coated spheres, Phys. Rev. B **73**, 075117 (2006).

[32] See Supplemental Material at http://link.aps.org/supplemental/10.1103/PhysRevB.104.035403 for a detailed description of the model.

[33] A. Bohr and B. R. Mottelson, *Nuclear Structure, Vol. II: Nuclear Deformations* (World Scientific, Singapore, 1998).

[34] P. Gulshani, Exact canonically conjugate momentum to the quadrupole tensor and microscopic derivation of the nuclear collective Hamiltonian, Phys. Lett. **77**, 131 (1978).

[35] S. Selstø and M. Førre, Alternative descriptions of the light-matter interaction beyond the dipole approximation, Phys. Rev. A **76**, 023427 (2007).

[36] C. Kittel, *Introduction to Solid State Physics* (Wiley, Hoboken, NJ, 2005).

[37] M. H. Cohen and F. Keffer, Dipolar sums in the primitive cubic lattices, Phys. Rev. **99**, 1128 (1955).

[38] K. Hepp and E. H. Lieb, On the superradiant phase transition for molecules in a quantized radiation field: The Dicke maser model, Ann. Phys. **76**, 360 (1973).

[39] S. Savasta, O. Di Stefano, and F. Nori, Thomas-Reiche-Kuhn (TRK) sum rule for interacting photons, Nanophotonics **10**, 465 (2020).

[40] M.-w. Xiao, Theory of transformation for the diagonalization of quadratic Hamiltonians, arXiv:0908.0787.

[41] K. Kolwas and A. Derkachova, Plasmonic abilities of gold and silver spherical nanoantennas in terms of size dependent multipolar resonance frequencies and plasmon damping rates, Opto-Electron. Rev. **18**, 429 (2010).

[42] M. Shopa, K. Kolwas, A. Derkachova, and G. Derkachov, Dipole and quadrupole surface plasmon resonance contributions in formation of near-field images of a gold nanosphere, Opto-Electron. Rev. **18**, 421 (2010).

[43] T. P. Doerr, O. I. Obolensky, and Y. K. Yu, Extending electrostatics of dielectric spheres to arbitrary charge distributions with applications to biosystems, Phys. Rev. E **96**, 062414 (2017).

[44] R. Yu, L. M. Liz-Marzán, and F. J. G. De Abajo, Universal analytical modeling of plasmonic nanoparticles, Chem. Soc. Rev. **46**, 6710 (2017).

[45] K. J. Savage, M. M. Hawkeye, R. Esteban, A. G. Borisov, J. Aizpurua, and J. J. Baumberg, Revealing the quantum regime in tunnelling plasmonics, Nature (London) **491**, 574 (2012).

[46] L. Sun, H. Lin, K. L. Kohlstedt, G. C. Schatz, and C. A. Mirkin, Design principles for photonic crystals based on plasmonic

nanoparticle superlattices, Proc. Natl. Acad. Sci. USA **115**, 7242 (2018).

[47] C.-P. Huang, X.-G. Yin, Q.-J. Wang, H. Huang, and Y.-Y. Zhu, Long-Wavelength Optical Properties of a Plasmonic Crystal, Phys. Rev. Lett. **104**, 016402 (2010).

[48] E. M. Purcell, H. C. Torrey, and R. V. Pound, Resonance absorption by nuclear magnetic moments in a solid, Phys. Rev. **69**, 37 (1946).

[49] C. Ciuti, G. Bastard, and I. Carusotto, Quantum vacuum properties of the intersubband cavity polariton field, Phys. Rev. B **72**, 115303 (2005).